Thermal response of iron and C-Mn steels with different ferrite/pearlite phase fraction under ultrasonic fatigue loading

Xiaoxue Pu, Johann Petit, Isabelle Darbord-Ranc, Danièle Wagner

Version of Record: https://www.sciencedirect.com/science/article/pii/S0921509319301789
Manuscript_b912f7af7d9b4ef9161626bd367dbc19

Thermal response of iron and C-Mn steels with different ferrite/pearlite phase fraction under ultrasonic fatigue loading

Xiaoxue Pu[a], Johann Petit[a], Isabelle Darbord–Ranc[a], Danièle Wagner[a,*]

[a] *LEME laboratory, Paris Nanterre University, 50 Rue de Sèvres, 92410 Ville d'Avray, France*

** Corresponding author: daniele.wagner@parisnanterre.fr*

Abstract

This work compares the thermal responses of an α-iron and two carbon steels (C12 and C65 steel) via in-situ infrared thermography under 20 kHz ultrasonic tension-compression fatigue testing. The α-iron has only ferrite phase, and C12 and C65 steels have ferrite-pearlite dual phases. During a series of interrupted self-heating tests, the surface temperature of the three materials increases gradually with stress amplitude, while the relation is non-linear. The increase of carbon content, inducing the pearlite phase percentage increasing, results in a lower temperature increase and higher fatigue strength. For the three materials, at a certain stress amplitude level, the specimen temperature suddenly increases to hundreds of degrees. Moreover, the dissipated energy per cycle is estimated based on the 1D heat diffusion equation and a power function between dissipated energy per cycle and stress amplitude is found. Finally, the mechanisms driving the observed thermal responses are discussed.

Keywords

Carbon-Manganese steel; Very High Cycle Fatigue (VHCF); self-heating, intrinsic dissipation; dissipative mechanisms; ultrasonic fatigue testing

1. Introduction

Since traditional experimental methods for estimating material fatigue strength are still costly and time-consuming, alternative approaches have been proposed, seeking for a rapid evaluation of fatigue properties of materials. Some of them are inclined to detect the physical processes of fatigue damage and failure of metallic specimens, based on their thermal responses during self-heating tests in high and very high cycle fatigue regimes. The self-heating test method relates fatigue strength and the intrinsic dissipated energy, therefore it is widely developed and applied in the fatigue field.

Materials under cyclic loading undergo a complex energy-conversion process

accompanying with materials degradation. Most of the lost energy is converted into heat causing the specimen temperature to rise. Researchers expect to take advantage of thermography to build a connection with materials properties under cyclic loading. In the 1970s, Reifsnider [1] and Charles [2] showed an attempt to use an infrared camera to measure the surface temperature during the tests and to predict the location of the impending fatigue cracks and map temperature field. Botny [3] presented the temperature profile with three characteristic stages: initial temperature increase, temperature stabilization and final rapid increase.

It can be easily checked during fatigue test that the specimen temperature depends on the stress amplitude. For loading frequency lower than 100 Hz and stress below the fatigue limit at 10^7 cycles, the temperature increase on specimen surface is generally very low (below 1 °C), but it remains superior to experimental noise and thermal resolution of conventional infrared cameras [4]. Hence, Luong [4,5] presented a "two-curves method" to interpolate experimental data from self-heating tests, one curve for stresses below the fatigue limit and the other one for stresses above the fatigue limit. Then, the corresponding intersection point was indicated as the fatigue limit. In these publications, the fatigue limit corresponds to the inflexion point of the S-N curve, standing around 10^7 cycles. Also, this fatigue limit can be considered as the transition between the High Cycle Fatigue regime (HCF) and the Very High Cycle Fatigue regime (VHCF), but doesn't represent the pure fatigue limit, below which no damage occurs. The Luong's method enables to observe the physical damage process, measure the intrinsic dissipation and rapidly evaluate the fatigue strength of the tested metals up to 10^7 cycles. These results were further developed and extended by Amiri and Khonsari [6], Cura *et al.* [7]. Amiri *et al.* [6] utilized an empirical equation to deduce the number of cycles of fatigue to failure as a function of the initial rate of temperature rise. Risitano *et al.* [8–10] proposed a "one-curve method" to rapidly estimate the fatigue limit of carbon steel (C30, C70 steels) by using the stabilization temperature under a low frequency tensile-compressive loading (10 Hz). The fatigue limit is determined by plotting the stabilization temperature against the applied stress and finding the intercept of the curve on the stress axis. The Luong's and Risitano's methods are the basis of fatigue properties determination methods by self-heating measurements developed by many authors [11–14].

In fact, the macroscopic characteristic evolution of materials is always accompanied with microstructural changes and the temperature variation could be considered as a consequence of these changes. Therefore, many researchers devote themselves to the calculation of energy dissipation to obtain the intrinsic data related to the material behavior. For this purpose, Chrysochoos *et al.* [15–18] developed an approach to determine the heat source development from a temperature field provided by an infrared camera. And then, the dissipative sources in fatigue process were estimated. Mareau *et al.* [19] proposed two rheological models to describe the dissipation mechanisms in almost 100% ferritic steel (with a few pearlitic areas)

under cyclic loading: the oscillation of pinned dislocations defined as an anelastic mechanism and the viscoplastic slip of dislocations considered as an inelastic mechanism. Subsequently, Munier [11] expanded this thought and performed the self-heating curves of sixteen steel grades. By using a two-scale probabilistic model, the authors showed that the observed two dissipative phenomena correspond to two dissipative mechanisms in low frequency cyclic loading in the HCF regime.

Results about the determination of fatigue limit in the HCF regime via thermographic methods brought a clear and incisive analysis to evaluate the fatigue life around 10^6 - 10^7 cycles. Owing to the recent development of high frequency ultrasonic machine, researches on high-frequency (20 kHz, 30 kHz) cyclic loading in VHCF domain are not very abundant yet. In the last few years, VHCF regime begins to draw more attention due to necessary component design up to 10^9 - 10^{11} cycles. Indeed, the fatigue tests performed after 10^6 cycles show a decrease of the fatigue limit with increasing number of cycles [20]. However, at high frequency, the strain rate sensitivity of materials can make their fatigue and thermal behaviors in VHCF regime different from the Low Cycle Fatigue (LCF) or HCF regimes [11,19]. In particular, materials can present a remarkable temperature increase under ultrasonic fatigue loading, compared with that in LCF or HCF regimes, while the test is still running. In most cases of LCF or HCF regimes, the specimen temperature is lower than dozens of degrees [5,8,11,14]. Nevertheless, the temperature field recording on the specimen surface during the fatigue tests can improve the understanding of damage evolution before the crack initiation at very low stress and strain amplitudes [21]. In the VHCF regime, the French ANR project DISFAT has given self-heating results on FCC and BCC materials [22]. For the strain rate-sensitive BCC materials, the self-heating response is more important than for FCC metals. Moreover, the dual phase steels with ferrite-pearlite or ferrite-martensite microstructure show an abnormal behavior at the higher stress amplitudes: a rapid increase of the surface temperature which doesn't correspond to the specimen fracture. Huang [23] has firstly shown this phenomenon on C-Mn ferrite-pearlitic steels, followed by Ranc *et al.* [24]. Torabian *et al.* [25] and recently by Ouarabi [26] on dual phase ferrite-martensitic steels, have also shown this phenomenon.

In this study, three steels (α-iron, C12 and C65) with incremental carbon content were used to investigate thermal response in self-heating tests under high-frequency ultrasonic fatigue loading (20 kHz). α-iron has only ferrite grains, while C12 and C65 are plain ferrite-pearlite dual-phase steels. The aim of this work is to explore the effect of carbon content on dissipated energy and to better understand the dissipative mechanisms.

2. Materials and experimental procedure

The studied materials were a polycrystalline α-iron and two dual-phase ferrite-pearlite steels (C12 and C65), whose carbon contents were 0.008 wt%, 0.03 wt%, and 0.61 wt%. The calculated mass percentage of ferrite and pearlite are given in table 1. The microstructure of each specimen surface was observed by optical microscopy (Fig.1). The bright grains were ferrite and the dark were pearlite. The received metal bars were machined into flat specimens with the thickness of 1 mm. The specimen geometry is shown in Fig.2. All the specimens were polished mechanically with a sequence of SiC papers (180#~2000#) before test.

The physical and mechanical properties of materials are presented in Table 2. Increase of carbon content (ferrite/pearlite phase ratio) enhances largely the strength and reduces the ductility. Thermal conductivity $\boldsymbol{k}$ and specific heat $\boldsymbol{C_p}$ were measured by the transient plane source method.

Table 1: Mass percentage of proeutectoid ferrite/pearlite phase.

Material	**Proeutectoid ferrite (wt%)**	**Pearlite (wt%)**
α-iron	100	0
C12	98.9	1.1
C65	16	84

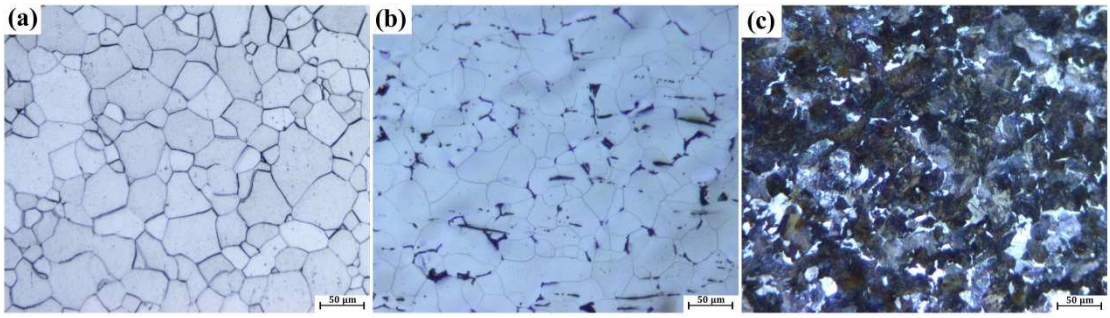

Fig.1 Microstructure of (a) α-iron, (b) C12 steel and (c) C65 steel.

Table 2: Physical properties of the three materials.

Material	**Lower yield stress (MPa)**	**Ultimate Tensile Stress (MPa)**	$\boldsymbol{C_p}$ **(J·kg^{-1}·K^{-1})**	$\boldsymbol{k}$ **(W·m^{-1}·K^{-1})**
α-iron	288	320	469	76.9
C12	357	446	458	60.7
C65	467	860	473	42.3

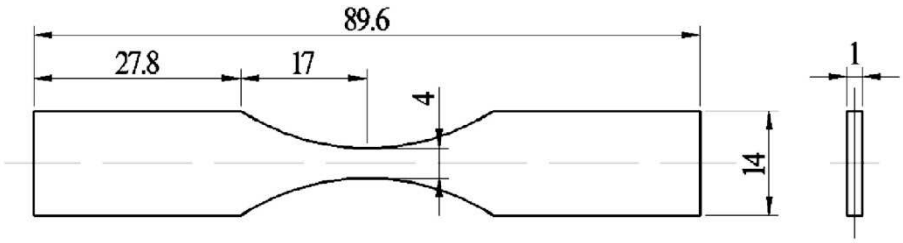

Fig.2 Dimensions of the ultrasonic fatigue test specimen (mm).

Fatigue tests were performed on a piezoelectric fatigue machine designed by C. Bathias *et al.* [27]. The resonance system was tuned to work at 20 kHz. The cyclic loading was tension-compression at a stress ratio R = -1. All the fatigue tests were carried out without cooling.

In order to record the temperature field on the specimen surface, an infrared (IR) camera Flir A325 was used. This is a microbolometer-based camera with a 320×240 detector and a thermal resolution (noise equivalent temperature difference, NETD) of 0.1 °C. The IR camera acquisition frequency was 3.75 Hz. The spectral range of the camera was between 7.5 and 13 μm and it can be used to record temperature from 0 °C to 350 °C. One side of the specimens was sprayed with a strongly emissive black paint to obtain a surface emissivity factor close to one.

Thus, the experimental setup, shown in Fig.3, consists of an ultrasonic fatigue machine, the IR camera set on one side of the specimen and also an optical microscope on the other side.. The microscope is composed of a CCD color camera surmounted by a microscope objective lens and will be used to follow the microstructural evolution of the specimens during ultrasonic fatigue testings.

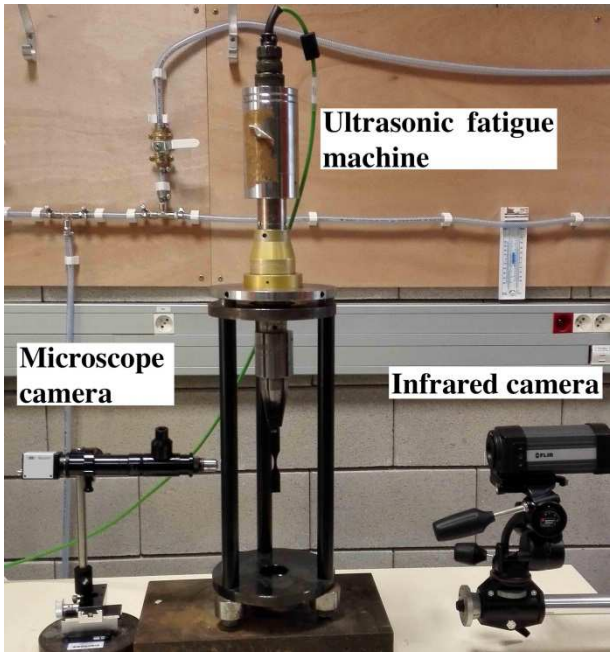

Fig.3 Experimental setup composed of the piezoelectric machine, the optical microscope

and the IR camera for damage evolution monitoring during ultrasonic fatigue testing.

Some interrupted self-heating tests were conducted on each steel, consisting of a series of cyclic loadings with an increase of stress amplitude. At each stress amplitude, a fatigue test was carried out up to 2.5×10^7 cycles and then interrupted. After the specimen cooled down to the room temperature, another loading step restarted.

3. Results

3.1. Temperature evolutions during self-heating tests

As mentioned previously, successive steps of the fatigue tests were conducted with increasing the stress amplitude and recording the temperature field at each step.

For instance, Fig.4a shows the temperature field on the specimen surface at a specific time and Fig.4b is the evolution of the temperature ΔT at the center of the specimen during one of the loading steps. Particularly, $\Delta T= \overline{T} - \overline{T}_{ini}$ is the mean temperature variation extracted from the rectangular zone in Fig.4a, where $\overline{T}$ is the mean absolute temperature through the rectangular zone and $\overline{T}_{ini}$ is the mean initial temperature of the specimen that is recorded each time before starting the tests.

According to the temperature evolution profile, two zones can be distinguished: first, the specimen temperature rapidly increases (stage I, $< 1\times10^7$ cycles) and then, it reaches the stabilization (stage II, $1\times10^7 \sim 2.5\times10^7$ cycles). The segmentation of stage I/II is based on the following two reasons. Firstly, when we magnify partly for all the temperature curves, in fact, the temperature at higher stress amplitudes remains increasing before 1×10^7 cycles, although this doesn't display so apparently in larger scale range. The complete stabilization is obtained after 1×10^7 cycles. Secondly, based on our still unpublished observations about PSBs appearance on α-iron surface, we find that the initial cycles of PSB emergence on α-iron at different stress amplitudes occur just before 1×10^7 cycles. So we infer that the stabilization stage ($>1\times10^7$ cycles) is related to the growth of embryonic PSBs and no occurrence of PSBs in other grains.

The stabilization of the temperature corresponds to the balance between the supplied external mechanical energy, the energy stored inside the material and the dissipated energy lost by convection, radiation at the specimen surface and conduction at the interface with the fatigue machine.

The evolutions of the temperature ΔT for some of the loading steps with different stress amplitudes are shown in Fig.5. This figure shows that by increasing the stress amplitude, regardless of the type of steel, the specimen temperature profile always evolves in the same way, as reported in Fig.4b. Nevertheless, the temperature level reached at stage II is observed to increase with the stress amplitude.

It is worth noting that in the case of α-iron loaded at 122 MPa, the temperature suddenly increases (Fig.5a) but no fracture was observed. Similarly, for C12 (Fig.5b) and C65 steels (Fig.5c), the specimen temperature also reaches several hundreds of degrees at 228 MPa and 230 MPa respectively, without specimen fracture. The infrared camera recording was stopped, because its upper measurement limit is 350 °C.

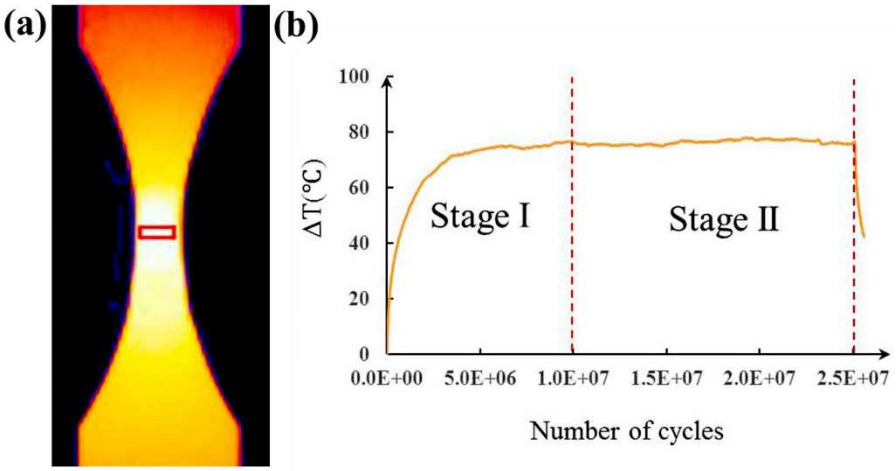

Fig.4 Loading step with σ_a = 106 MPa for α-iron (a) temperature field on specimen surface at N=2.5×10^7 cycles (b) temperature evolution versus number of fatigue cycles.

For each loading step in Fig.5a-c, the stabilized temperatures reached during stage II are plotted for the three steels in Fig.5d. Fig.5d shows that the temperature elevation ΔT increases gradually by increasing the stress amplitude. The relation of stress amplitude and temperature elevation is obviously non-linear. The maximum stabilized temperature increase ΔT before the sudden increase is ~90 °C for iron, ~75 °C for C12, and ~60 °C for C65 and ~100 °C for iron, ~90°C for C12, and ~70°C for C65 at the moment of the sudden increase.

Fig.6 collects statistics of the slopes of the temperature profiles obtained in stage II (from 1×10^7 to 2.5×10^7 cycles) from several self-heating tests. Each data point respectively denotes the mean value and its standard deviation along stage II. It can be seen that stabilization slopes at stage II for all materials are generally rather small and can be negligible. It can be verified that the specimen temperatures in self-heating tests are completely stable until 2.5×10^7 cycles, except for the last stress level. Fig.7 shows the conventional S-N curve obtained without cooling of the α-iron, C12 steel and C65 steel. Their fatigue limit at 2×10^9 cycles can be deduced to be 107 MPa, 190 MPa and 210 MPa, respectively.

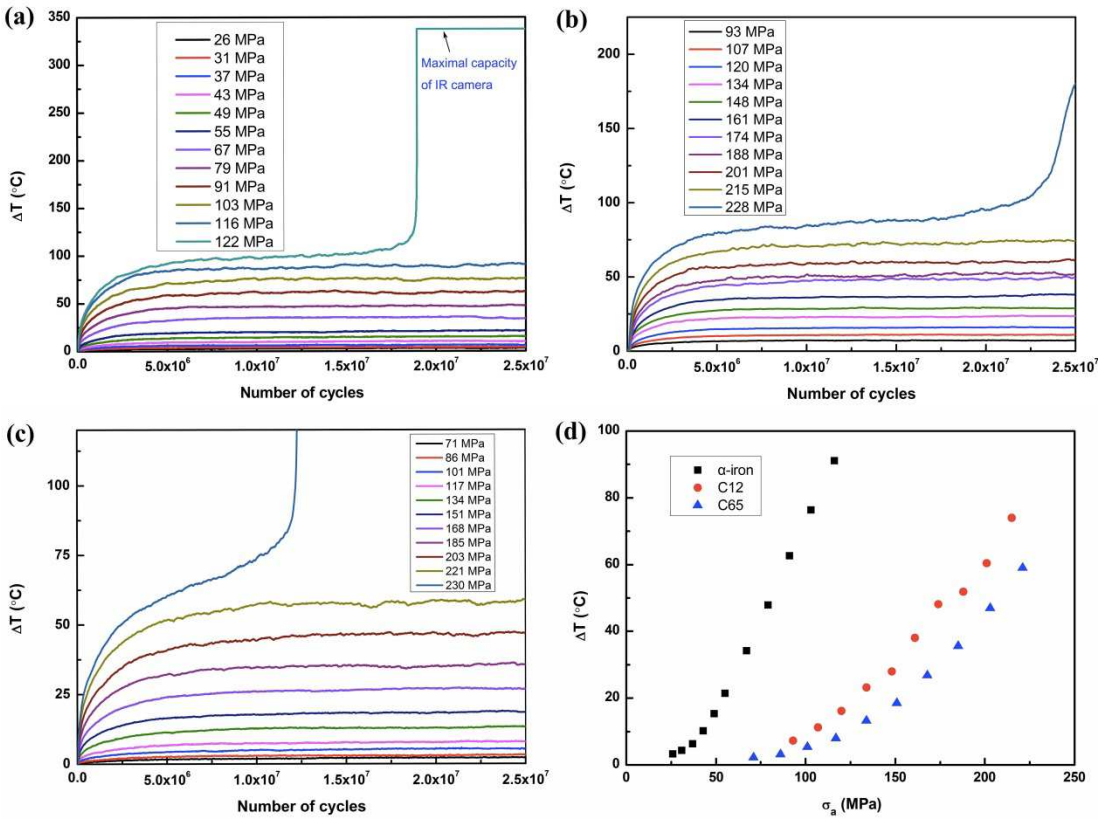

Fig.5 Temperature evolution versus number of cycles under different stress amplitude for (a) α-iron, (b) C12 steel, (c) C65 steel. (d) The temperature increase at stabilization stage (stage II) versus stress amplitude under ultrasonic fatigue tests.

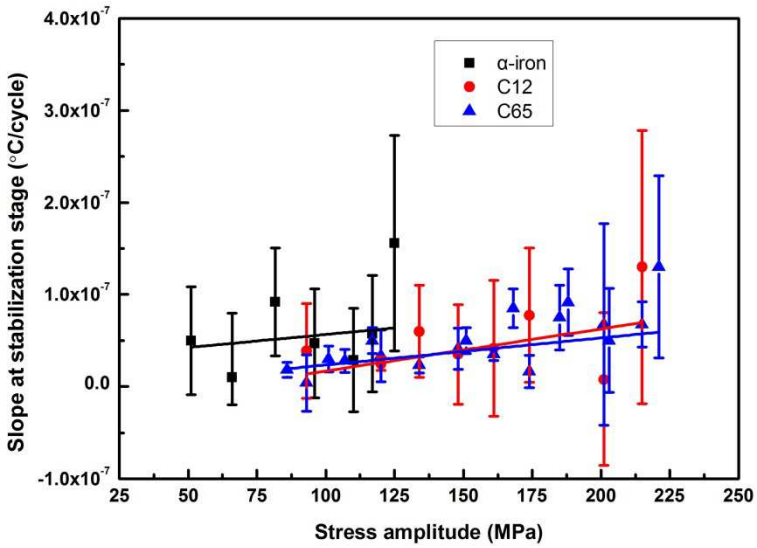

Fig.6 Mean slopes of temperature profiles measured along the stabilization stage (stage II, $1\times10^7 \sim 2.5\times10^7$ cycles) in self-heating tests for α-iron, C12 and C65.

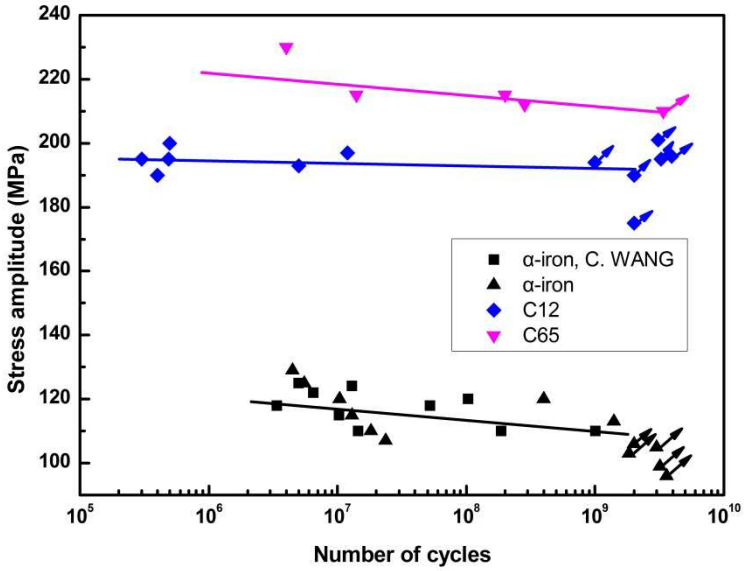

Fig.7 Traditional S-N curves of α-iron, C12 and C65. The black square points of iron come from C.WANG [28].

3.2. Heat source estimations

In this study, the heat diffusion equation proposed by Chrysochoos *et al*. [29] was used to estimate the intrinsic dissipation from temperature measurements. Assuming that materials properties like mass density ρ, thermal conductivity k and specific heat C_p were independent of the thermodynamic state, also assuming there is no temperature-induced microstructural change and neglecting the convective terms, the heat diffusion equation is written as:

$$\rho C_p \dot{\theta} + \mathrm{div}(-k\overrightarrow{\mathrm{grad}}(\theta)) = S_{the} + d_1 \tag{1}$$

In this equation, $\theta = \mathrm{T} - \mathrm{T_{ini}}$, with T and $\mathrm{T_{ini}}$ the local instantaneous and initial absolute temperatures respectively. $\dot{\theta}$ denotes the local temperature time derivative. S_{the} represents the thermoelastic sources. In the steady-state heat transfer, S_{the} is null over one cycle. d_1 is the intrinsic dissipation.

With $\theta(x,t)$ denoting the mean temperature variation at time t over the section $S(x)$, and x being the longitudinal coordinate, the 1D heat diffusion equation can be formulated as [30]:

$$\rho C_p \left(\frac{\partial \theta}{\partial t} + \frac{\theta}{\tau^{1D}(x)}\right) - k\left(\frac{S'}{S}\frac{\partial \theta}{\partial x} + \frac{\partial^2 \theta}{\partial x^2}\right) = d_1(x,t) \tag{2}$$

where $d_1(x,t)$ is the longitudinal distribution of the mean heat source per cross section S and S' is the spatial derivative of S. $\tau^{1D}(x)$ being a time constant characterizing heat losses through the specimen surface, it is defined as:

$$\tau^{1D}(x) = \frac{\rho C_p S(x)}{2h(e+l(x))} = \frac{\rho C_p e l(x)}{2h(e+l(x))} \tag{3}$$

where h is the heat exchange coefficient taken into account for the convection and radiation effects, e is the thickness of specimen and $l(x)$ is its variable width.

When dividing equation (2) by ρC_p, the thermal diffusivity $D = \frac{k}{\rho C_p}$ appears in the equation and the source term can be expressed as $\tilde{d}_1 = \frac{d_1(x,t)}{\rho C_p}$ (^{o}C/s).

The mean dissipated energy per cycle can be obtained as $\frac{\tilde{d}_1(x,t)}{f}$, where f is the loading frequency. Then, the maximum heat source, taken at the center of the specimen during stage II, is expressed as $\frac{\tilde{d}_1}{f}$ (^{o}C/cycle).

Fig.8 shows the measured dissipated energy per cycle as a function of stress amplitude, calculated from equation (2). The higher stress amplitude produces the higher dissipated energy. At a given stress amplitude, α-iron always dissipates the most thermal energy, while C65 steel releases the least. The curves can be well fitted by the power function, and it can be noticed that their power exponent increases with pearlite phase percentage (depending on carbon content).

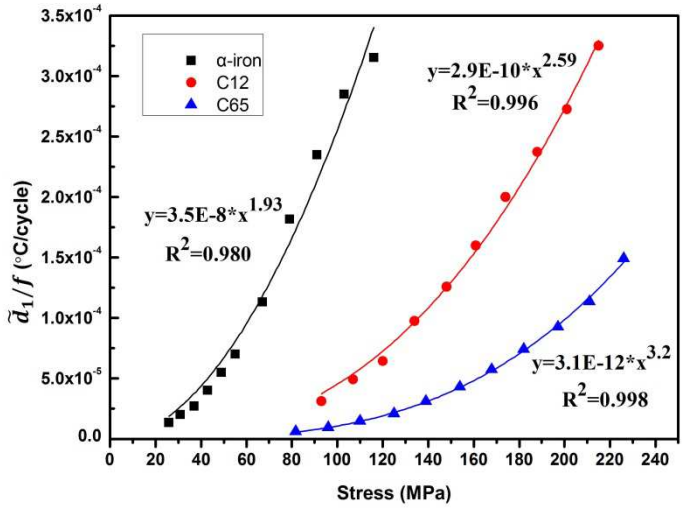

Fig.8 Dissipated energy per cycle versus stress amplitude under ultrasonic loading. The solid points are calculated from equation (2) at 2.5×10^7 cycles.

4. Discussion

The following sections discuss about the mechanisms implied at different ranges of the stress amplitude, the links between the dissipation versus the stress amplitude, and the influence of the ferrite/pearlite phase fraction (depending on carbon content) to dissipation energy for α-iron, C12 and C65 steels.

4.1. High stress amplitudes

In order to investigate the relevant mechanisms about the sudden temperature increase in self-heating tests, a new specimen of α-iron was loaded to a stress amplitude of 106 MPa during 2×10^9 cycles while recording the temperature field and the microstructure evolution as previously described in section 2. The Fig.9 gives the temperature evolution at the center of the specimen (average on the rectangular zone illustrated in Fig.4a) and the corresponding persistent slips bands (PSBs) evolutions. The first PSBs occur in few grains (image ①). From the image ③, a sudden temperature rise to hundreds of degrees happens, with the rapid increase of the surface PSBs density.

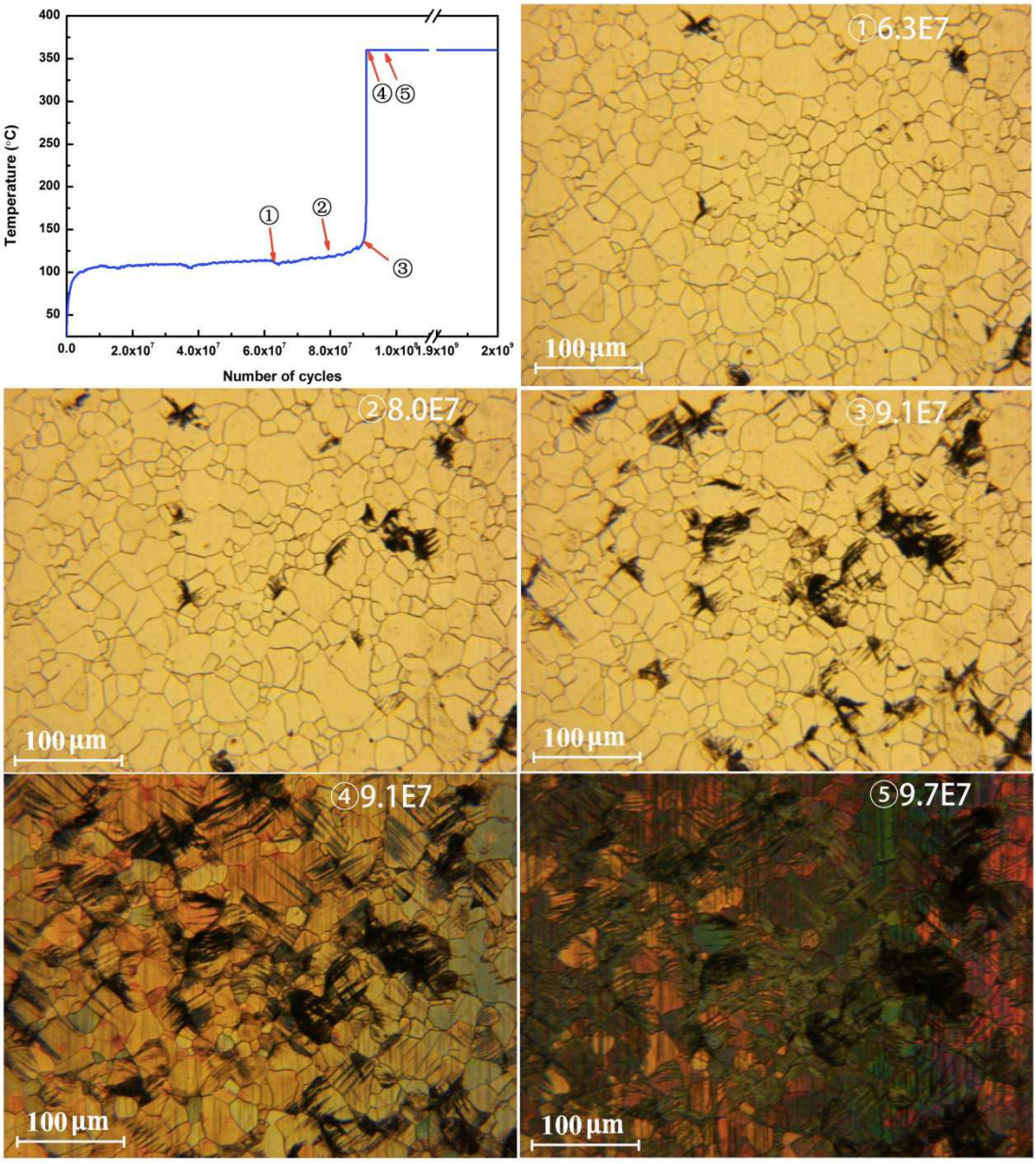

Fig.9 Temperature evolution and corresponding microstructure evolution showing the PSBs

multiplication along the test of α-iron at 106 MPa.

At the image ⑤, the whole camera field is full of PSBs. So, no PSBs localization occurs and the specimen still survives at high temperature. That indicates that the steep rise in temperature is not related to crack initiation. Furthermore, due to oxidation at high temperature, the specimen color is observed to change.

Marks of the dislocation glide are visible on the specimen surface, but the irreversible microstructure changes also appear in the bulk. This assertion was checked by cutting the α-iron specimen (whose the loading history is given in Fig.5a) in the center which experiences the sudden temperature increase at 122 MPa from 2×10^7 cycles to 2.5×10^7 cycles. Fig.10 displays its cross-section after cutting. Before SEM observation, the cross-section is prepared by gentle polishing and etching by 4% Nital solution. There are numerous well-ordered micro-voids in some grains, while no damage appears in some other grains. The damage grains are surely well-oriented grains with high Schmid factor. An attempt to measure crystal orientation by EBSD failed because of the too much deformed cross-section which considerably decreases the signal-to-noise ratio. Furthermore, it can be observed in each damaged grain, that the micro-voids are assembled along straight lines, going through all the grain and preferentially orientated, depending on the grain. These long streaks of micro-voids can sometimes cross the grain boundaries as observed Fig.10b. It can be reasonably assumed that the crossing occurs between two low misorientated adjacent grains. This deformation mode reminds the classic mechanisms related to the primary hardening stage in polycrystals. The traces of vacancies or voids are possible to be caused by the movement of jogged screw dislocations [31].

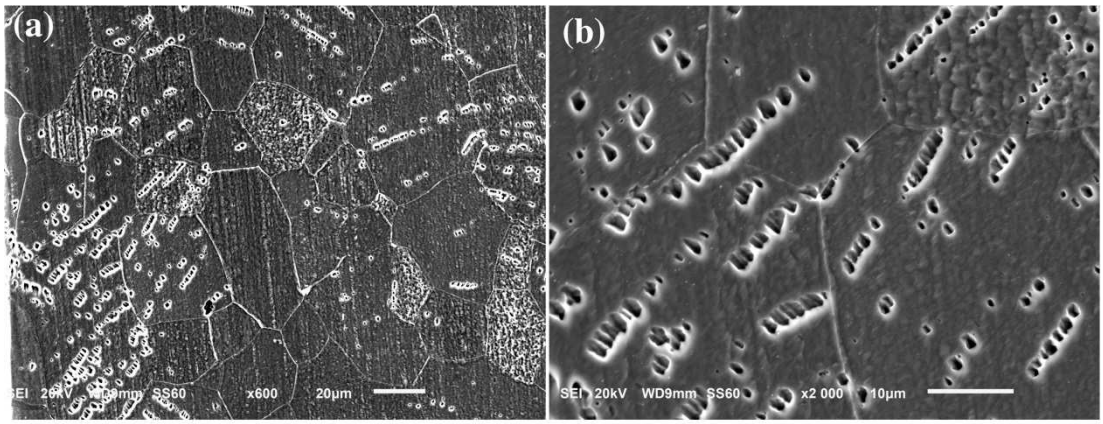

Fig.10 (a) Cross-section of α-iron specimen after experiencing the sudden temperature increase. (b) Magnification of the internal damage in left picture.

As reported previously by others authors [23–26], these BCC steels show an abnormal increase above a certain stress amplitude. For Torabian et al. [25] for dual phase ferrite-martensitic steels this behavior is due to the change of deformation mode

from thermally activated deformation mode to the athermal deformation mode. Indeed, Mughrabi *et al.* [32] described the temperature-dependent deformation of BCC metals by a schematic diagram as shown in Fig.11. The deformation mechanisms are classified by the transition temperature T_0. Below the transition temperature T_0, it's named as "thermally activated regime" or "thermal regime", and above T_0, it's called "athermal regime". Below T_0, at low temperature, the screw dislocations are nearly immobile and the dislocation glide occurs mainly by the to-and-fro glide of edge dislocations. Above T_0, the mobilities of edge and screw dislocations become comparable and screw dislocations can cross slips easily. Whether materials can carry out screw dislocations multiplication, the transition from thermal regime to athermal regime occurs.

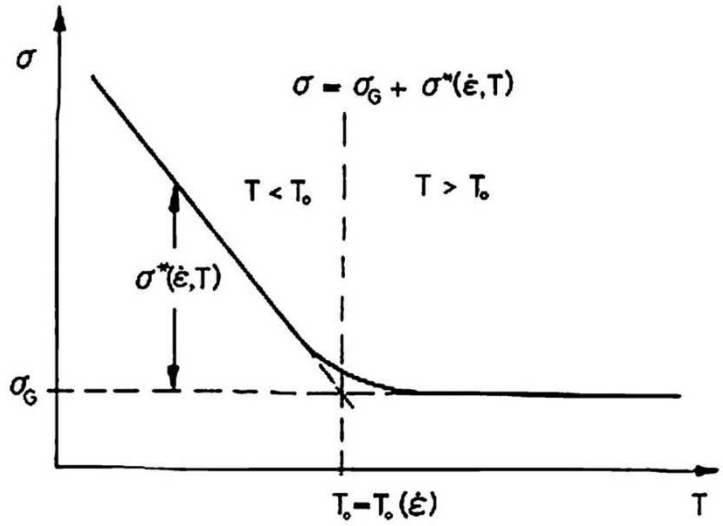

Fig.11 Schematic diagram of flow stress of BCC metals versus temperature, cf. [32].

Flow stress $\sigma = \sigma(T, \dot{\varepsilon})$ is defined as the instantaneous value of the stress required to continue plastically deforming the material. It depends on strain rate $\dot{\varepsilon}$, and temperature T [33] for any plastic strain and it can be written as the sum of an athermal stress σ_G and a thermal stress $\sigma^*(T, \dot{\varepsilon})$:

$$\sigma(T, \dot{\varepsilon}) = \sigma_G + \sigma^*(T, \dot{\varepsilon}) \quad (4)$$

Flow stress increases non-linearly with increasing strain rate [34,35]. For α-iron [34,35], below 10^3 s^{-1}, flow stress increases with increasing strain rate, but decreases with increasing temperature [36,37]. Generally, flow stress greatly depends on temperature. For a given stress rate, flow stress decreases as the temperature rises and levels off to the athermal stress σ_G. The critical temperature from thermal stress to athermal stress is the transition temperature T_0. The transition temperature T_0 would be affected only by strain rate [38]. Under 20 kHz ultrasonic loading, strain rate lies around $10\sim10^2$ s^{-1}, higher than those ($10^{-3}\sim10^{-2}$ s^{-1}) generally encountered in the LCF and HCF regimes. The high strain rate leads to transition temperature T_0 between the

thermally activated regime and the athermal regime for BCC metals [32] far higher than room temperature. In the flow behavior diagram of 0.12 wt% carbon steel given by Campbell and Ferguson [38], T_0 increases from 25 °C to 100 °C with strain rate from 0.01 s^{-1} to 1 s^{-1} and continue increasing above 200 °C when the strain rate reaches 100 s^{-1}.

On the basis of optical observations during the fatigue tests and on post-mortem specimen, it is rational to consider that the sudden temperature rise to hundreds of degrees in Fig.5 is caused by multiplication of screw dislocations, corresponding to the transition between thermal and athermal regimes. The multiplication leads to the formation of a lot of PSBs.

Another point, which was not taken into account in the previous works, is that the yield stress at hundreds of degrees drops greatly compared to that at room temperature with the shortening and then the disappearance of the Lüders plateau. Screw dislocations are easier to cross slips above yield stress. As reported by the Fig.12, for a carbon manganese steel with 0.2% of carbon, the yield stress decreases from 300 MPa to 150 MPa with the disappearance of the Lüders plateau when the temperature increases from 20 °C to 300 °C.

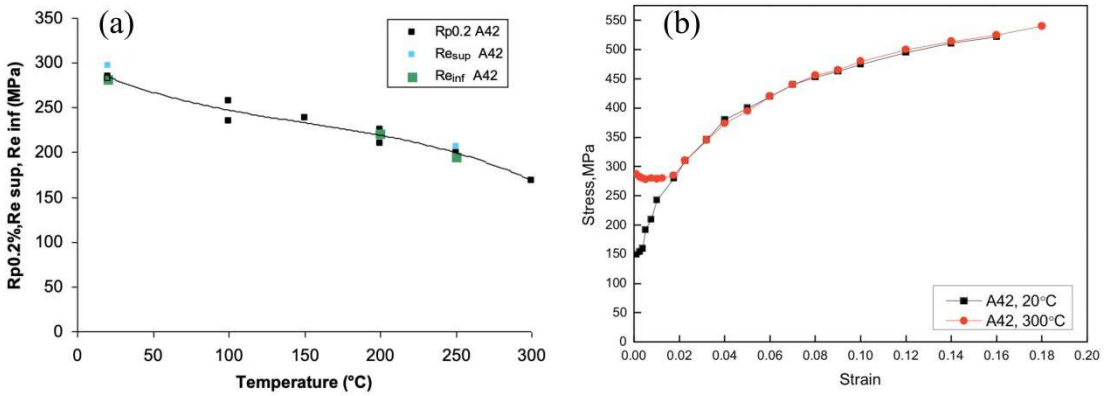

Fig.12 (a) 0.2% proof stress (Rp0.2), upper yield stress (Re_{sup}) and lower yield stress (Re_{inf}) of French standard A42 steel. (b) Uniaxial tensile curve of the same steel at room temperature and high temperature. [39]

The disappearance of the Lüders plateau with the temperature increase probably accelerates this phenomenon. Indeed, at a given stress amplitude σ_a, the ratio σ_a over yield stress (Re_{sup}, Re_{inf}) increases with temperature.

In addition, the temperature corresponding to the sudden increase is around 100 °C for α-iron and C12. This temperature corresponds to the beginning of dynamic strain aging in quasi-static tensile tests [40], caused by the increase of the carbon and nitrogen atoms diffusion rate in the iron solid solution. At this temperature the solute atoms are not yet obstacles to the dislocation gliding and can follow the dislocation. More dislocations can glide and the self-heating temperature increases.

The same test was performed on the C12 steel at a stress amplitude of 216 MPa

until 3×10^9 cycles. The same result could be found with a sudden temperature increase during which the PSBs density rapidly multiplies.

So, it can be assumed that for ferrite-pearlite steels, as for ferrite–martensitic steels, the sudden temperature increase in self-heating tests is due to:

- the ferrite phase in which the transition from the thermal regime to the athermal regime occurs. In pure martensitic steels, the sudden temperature increase doesn't occur [41];
- the yield stress which decreases with the temperature;
- and the diffusion rate of carbon and nitrogen atoms in solid solution which increases with temperature above 100 °C.

4.2. Low stress amplitudes

In this part, we discuss about the microstructural changes at low stress amplitude which will not cause the sudden temperature increase to hundreds of degrees. As an example, a new specimen of α-iron tested at 105 MPa is presented in Fig.13. The specimen temperature doesn't experience the sudden temperature increase even up to 3×10^9 cycles and only few PSBs appear on the surface. No visible micro-voids can be found inside the specimen. Furthermore, at lower stress amplitude (103 MPa, 80 MPa), α-iron specimens show neither the PSBs on the surface nor the visible micro-voids in the bulk.

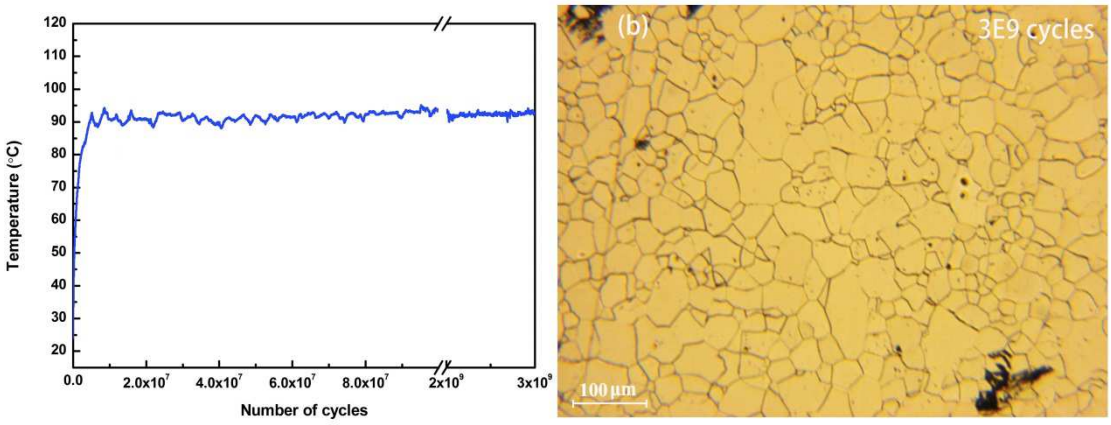

Fig.13 The case of α-iron at 105 MPa showing (a) its temperature evolution without sudden increase until 3×10^9 cycles and (b) the PSBs configuration on the surface after 3×10^9 cycles.

Therefore, we can suppose that in thermal regime, mainly edge dislocations glide. The thermal changes (Fig.5d) in thermal regime are associated with the activation of more slip systems and the increase of irreversible dislocation gliding. It's possible to produce few rare PSBs or completely no PSBs. Fig.6 is the slope of the stabilized temperature from 1×10^7 to 2.5×10^7 cycles which is close to zero all along stage II.

That means the cumulative hardening of edge dislocation gliding is very low, the heat sources originate from mainly edge dislocations and their intensity remains nearly constant.

According to Eq. (4), the dominant contribution to σ^* arises from the lattice friction stress (comparable to the Peierls-Nabarro stress) experienced by dislocations, while the athermal component σ_G arises from the elastic interaction of the dislocations during glide (comparable to the stress needed to drag dislocations through the forest) and is usually related to the dislocation density ρ, as [42]:

$$\sigma_G = \alpha G b \sqrt{\rho} \tag{5}$$

Finally, the Taylor equation described the relationship between flow stress and dislocation density:

$$\sigma = \sigma_0 + \alpha G b \sqrt{\rho} \tag{6}$$

where σ_0 is the lattice friction stress, α a geometrical constant (α ~ 0.1-0.4) depending on the dislocation arrangement, G the shear modulus, and b the modulus of the Burgers vector. The Eq. (6) manifests that flow stress increases with the dislocations density.

So, at low stress amplitude in 20 kHz fatigue testing, heat dissipation mainly comes from reversible dislocation movements. From a certain stress amplitude σ_a, the flow stress is reached in some well-orientated grains and irreversible dislocations can move, increasing σ_G through the dislocation density ρ. Thereafter, when the macroscopic applied stress increases, local stresses reach the flow stress in more and more grains. Hence, the material heats up more and more (heat transfers with exterior tend to saturate), causing $\sigma^*(T, \dot{\varepsilon})$ to decrease. Consequently, the flow stress is controlled by two antagonistic effects: the increase of σ_G with the stress amplitude and the decrease of $\sigma^*(T, \dot{\varepsilon})$ with the rise in temperature. At higher stress (but still far below the yield stress R_e), the temperature keeps rising, causing $\sigma^*(T, \dot{\varepsilon})$ to drop faster than σ_G to increase. Then, when the temperature reaches T_0 (roughly 100 °C for the three materials), screw dislocations can easily glide and the plastic deformation becomes catastrophic, resulting in a very steep and important temperature increase. As mentioned in the previous paragraph, the diffusion rate of solute atoms and the yield stress reduction with the temperature most likely contribute to the plastic deformation acceleration.

4.3. Dissipative Mechanisms and estimation

In low frequency fatigue tests, microplastic deformation at low stress amplitude is negligible, since the screw dislocations are nearly immobile. The dislocation gliding occurs mainly by the quasi-reversible glide of edge dislocations (except on the specimen surface). Multiplication of dislocations is largely suppressed and there is no or little cyclic hardening. This motion is quasi-reversible after unloading and it can be

labeled as anelasticity from a macroscopic viewpoint. At higher stress amplitude, microplastic deformation occurs: the glide of screw dislocations increases and accumulates massively. Dislocations become irreversible after unloading or even a fully reversed loading. It can be labeled as inelasticity. [19,25,31]

In previous works about high frequency fatigue tests [25], mechanical behavior of BCC steels in fatigue can also be classified into the two states: anelasticity and inelasticity. At stress amplitudes in athermal regime, the screw dislocation is fully activated in most grains. The continuous multiplication of screw dislocation results in a heat dissipation and temperature elevation. The (macroscopic) behavior of the athermal regime is clearly inelastic. While, for the stress amplitude in thermal regime, screw dislocations gliding is suppressed or largely limited. The macroscopic behavior in this regime can be denoted as anelasticity. Based on this assumption, a quadratic formula was used to describe the relationship between intrinsic dissipation and stress amplitude.

In Fig.8, the tendency of dissipated energy per cycle always increase with stress amplitude, consistent with other materials in LCF and HCF domains [11,19] and in VHCF domain [25]. In our work as shown in Fig.8, the evolutions of dissipated energy per cycle with stress amplitudes are observed to be power laws.

According to the thermodynamic theory, in particular the Clausius-Duhem inequality, the intrinsic dissipation energy d_1 is the product of the total plastic energy minus the stored energy. As proposed by Chrysochoos [43], d_1 is expressed as the following equation:

$$d_1 = \sigma : \dot{\varepsilon}_P - X : \dot{\alpha} - R\dot{p} \approx \beta\sigma\dot{\varepsilon}_P \quad (\beta<1) \tag{7}$$

where, (X, α) and (R, p) are the couples (thermodynamical force, state variable) associated with the kinematical and isotropic hardening, respectively. β is the Taylor-Quinney coefficient, representing the proportion of plastic energy to be dissipated. For steel materials in tensile tests, the value of β tends to be 0.5~0.8 [43–45]. Along stage II, β can be considered as a constant value per cycle, since temperature is stabilized and the thermal and mechanical boundary conditions don't vary.

Furthermore, the relation between plastic strain rate and the stress amplitude is assumed to satisfy a Norton flow rule [46]:

$$\dot{\varepsilon}_{\mathrm{p}} = \left(\frac{\sigma}{\mathrm{K}}\right)^{n} \tag{8}$$

Therefore, combining the Eq. (7) and (8), the intrinsic dissipation energy in one cycle can be expressed as a power function of stress amplitude:

$$d_1 = \mathrm{C}(\sigma)^{m} \tag{9}$$

where, C is related to the parameter K and β, and $m = n + 1$. The results in Fig.8 show that the power fitting is in good agreement with the above Eq. (9) and the power exponents of the fitting increase with pearlite percentage.

4.4. Effect of ferrite/pearlite fraction

The α-iron, C12 and C65 steels, differ from each other due to differences in carbon content, or more precisely by the ferrite/pearlite ratio. Pearlite phase percentage greatly affects the physical properties, such as thermal conductivity, mechanical properties, such as (Table 2) yield stress, Ultimate Tensile Stress (UTS), elongation at break, and the dissipative behaviors. For example, with carbon content increasing, the micro-hardness of ferrite grains for α-iron, C12 and C65 are 179 HV, 197 HV and 243 HV, respectively.

The fatigue limits at 2×10^9 cycles of these three materials (α-iron, C12 and C65) found in conventional S-N curves are 105 MPa, 210 MPa and 220 MPa, respectively.

The resistance to plastic flow increases with carbon content and pearlite phase percentage. The minimum stress amplitude for each material which causes the sudden temperature elevation in Fig.5a-c also increases with pearlite fraction. In Fig.5a-c, the maximum stabilization temperatures ΔT in thermal regime of α-iron, C12 and C65 steel respectively lie around ~90 °C, ~75 °C and ~60 °C. The temperature ΔT may correspond to the transition temperature T_0. Consequently, T0 is possible to be remarked to decrease with carbon content.

Dissipative behaviors depend upon the material microstructure. As the hardness of pearlite is much higher than ferrite, dislocations preferentially glide in the soft ferrite phase. Irrespective of the texture and the grain size, ferrite phase fraction is the main reason why the dissipated energy of these three steels (α-iron, C12, C65) lowers respectively.

5. Conclusions

The thermal responses of three steels with different carbon contents, α-iron (0.008 wt%), C12 (0.03 wt%) and C65 (0.61 wt%), under high-frequency ultrasonic fatigue loading, are compared.

More carbon content (or higher pearlite percentage) in steels leads to lower thermal conductivity and produces higher fatigue strength. In self-heating tests, with carbon content increasing (i.e. ferrite percentage decreasing), the temperature elevation and dissipated energy decline.

For the three steels, it has been found that the stress amplitude at which specimens undergo a sudden temperature up to hundreds of degrees in ΔT-N curves mainly corresponds to the transition from thermally-activated regime to the athermal regime in BCC metals under high frequency fatigue loading. The occurrence of the dynamic strain ageing above 100 °C and the yield stress decrease with temperature also contribute to the rapid accumulation of PSBs, internal damage and significant rise in temperature.

-Below the transition temperature T_0 between the two regimes, the strain behavior is mainly caused by edge dislocations, and screw dislocations multiplication is largely suppressed. The increase of stress amplitude leads to the increase of irreversible

dislocations gliding, producing a non-linear rise in ΔT-σ_a curves of these three materials. The dissipated energy per cycle also displays the power evolution with stress amplitude, where the exponent is observed to increase with the pearlite percentage.

-Above T_0, the multiplication of screw dislocations takes place and it is possible to cause final failure at a certain cycles in the VHCF domain.

The sudden increase enhanced by the yield stress drop is possible to be related with the diffusion rate increase of solute atoms (C, N) as the temperature increases.

Acknowledgements

We thank the financial support from China Scholarship Council for doctoral student PU Xiaoxue.

References

[1] K.L. Reifsnider, R.S. Williams, Determination of fatigue-related heat emission in composite materials, Experimental Mechanics. 14 (1974) 479–485. doi:10.1007/BF02323148.

[2] J.A. Charles, F.J. Appl, J.E. Francis, Using the scanning infrared camera in experimental fatigue studies, Experimental Mechanics. 15 (1975) 133–138. doi:10.1007/BF02318849.

[3] R. Botny, J. Kaleta, A method for determining the heat energy of the fatigue process in metals under uniaxial stress: Part 1. Determination of the amount of heat liberated from a fatigue-tested specimen, International Journal of Fatigue. 8 (1986) 29–33. doi:10.1016/0142-1123(86)90044-7.

[4] M.P. Luong, Fatigue limit evaluation of metals using an infrared thermographic technique, Mechanics of Materials. 28 (1998) 155–163. doi:10.1016/S0167-6636(97)00047-1.

[5] M.P. Luong, Infrared thermographic scanning of fatigue in metals, Nuclear Engineering and Design. 158 (1995) 363–376. doi:10.1016/0029-5493(95)01043-H.

[6] M. Amiri, M.M. Khonsari, Life prediction of metals undergoing fatigue load based on temperature evolution, Materials Science and Engineering: A. 527 (2010) 1555–1559. doi:10.1016/j.msea.2009.10.025.

[7] F. Cura, G. Curti, R. Sesana, A new iteration method for the thermographic determination of fatigue limit in steels, International Journal of Fatigue. 27 (2005) 453–459. doi:10.1016/j.ijfatigue.2003.12.009.

[8] G. La Rosa, A. Risitano, Thermographic methodology for rapid determination of the fatigue limit of materials and mechanical components, International Journal of Fatigue. 22 (2000) 65–73. doi:10.1016/S0142-1123(99)00088-2.

[9] A. Risitano, G. Risitano, Cumulative damage evaluation of steel using infrared thermography, Theoretical and Applied Fracture Mechanics. 54 (2010) 82–90. doi:10.1016/j.tafmec.2010.10.002.

[10] A. Risitano, G. Risitano, Cumulative damage evaluation in multiple cycle fatigue tests taking into account energy parameters, International Journal of Fatigue. 48 (2013) 214–222. doi:10.1016/j.ijfatigue.2012.10.020.

[11] R. Munier, C. Doudard, S. Calloch, B. Weber, Determination of high cycle fatigue properties of a wide range of steel sheet grades from self-heating measurements, International Journal of Fatigue. 63 (2014) 46–61. doi:10.1016/j.ijfatigue.2014.01.004.

[12] C. Doudard, M. Poncelet, S. Calloch, C. Boue, F. Hild, A. Galtier, Determination of an HCF criterion by thermal measurements under biaxial cyclic loading, International Journal of Fatigue. 29 (2007) 748–757. doi:10.1016/j.ijfatigue.2006.06.009.

[13] J. Huang, M.-L. Pastor, C. Garnier, X. Gong, Rapid evaluation of fatigue limit on thermographic data analysis, International Journal of Fatigue. 104 (2017) 293–301. doi:10.1016/j.ijfatigue.2017.07.029.
[14] Q. Guo, X. Guo, Research on high-cycle fatigue behavior of FV520B stainless steel based on intrinsic dissipation, Materials & Design. 90 (2016) 248–255. doi:10.1016/j.matdes.2015.10.103.
[15] T. Boulanger, A. Chrysochoos, C. Mabru, A. Galtier, Calorimetric analysis of dissipative and thermoelastic effects associated with the fatigue behavior of steels, International Journal of Fatigue. 26 (2004) 221–229. doi:10.1016/S0142-1123(03)00171-3.
[16] A.E. Morabito, A. Chrysochoos, V. Dattoma, U. Galietti, Analysis of heat sources accompanying the fatigue of 2024 T3 aluminium alloys, International Journal of Fatigue. 29 (2007) 977–984. doi:10.1016/j.ijfatigue.2006.06.015.
[17] S. Giancane, A. Chrysochoos, V. Dattoma, B. Wattrisse, Deformation and dissipated energies for high cycle fatigue of 2024-T3 aluminium alloy, Theoretical and Applied Fracture Mechanics. 52 (2009) 117–121. doi:10.1016/j.tafmec.2009.08.004.
[18] A. Chrysochoos, H. Louche, An infrared image processing to analyse the calorific effects accompanying strain localisation, International Journal of Engineering Science. 38 (2000) 1759–1788. doi:10.1016/S0020-7225(00)00002-1.
[19] C. Mareau, Influence of the free surface and the mean stress on the heat dissipation in steels under cyclic loading, International Journal of Fatigue. 31 (2009) 1407–1412. doi:10.1016/j.ijfatigue.2009.03.022.
[20] C. Bathias, There is no infinite fatigue life in metallic materials, Fatigue & Fracture of Engineering Materials & Structures. 22 (n.d.) 559–565. doi:10.1046/j.1460-2695.1999.00183.x.
[21] D. Wagner, N. Ranc, C. Bathias, P.C. Paris, Fatigue crack initiation detection by an infrared thermography method, Fatigue & Fracture of Engineering Materials & Structures. 33 (n.d.) 12–21. doi:10.1111/j.1460-2695.2009.01410.x.
[22] V. Favier, A. Blanche, C. Wang, N.L. Phung, N. Ranc, D. Wagner, C. Bathias, A. Chrysochoos, H. Mughrabi, Very high cycle fatigue for single phase ductile materials: Comparison between α-iron, copper and α-brass polycrystals, International Journal of Fatigue. 93 (2016) 326–338. doi:10.1016/j.ijfatigue.2016.05.034.
[23] Z.Y. Huang, N. Ranc, D. Wagner, Dislocations gliding study by IR thermography in C-Mn steels with different solute atoms content in the gigacycle fatigue domain, Key Engineering Materials. (2016). doi:10.4028/www.scientific.net/KEM.664.177.
[24] N. Ranc, V. Favier, B. Munier, F. Vales, G. Thoquenne, F. Lefebvre, Thermal Response of C45 Steel in High and Very High Cycle Fatigue, Procedia Engineering. 133 (2015) 265–271. doi:10.1016/j.proeng.2015.12.668.
[25] N. Torabian, V. Favier, S. Ziaei-Rad, J. Dirrenberger, F. Adamski, N. Ranc, Thermal response of DP600 dual-phase steel under ultrasonic fatigue loading,

Materials Science and Engineering: A. 677 (2016) 97–105. doi:10.1016/j.msea.2016.09.025.
[26] M. Ouarabi, Influence de la fréquence de chargement sur la résistance à l'amorçage et la croissance de fissure de fatigue dans des aciers utilisés pour des applications mécaniques exigeantes, PhD dissertation, Université Paris Nanterre, 2018.
[27] C. Bathias, P.C. Paris, Gigacycle fatigue in mechanical practice, CRC press, New York, 2005.
[28] C. Wang, Microplasticité et dissipation en fatigue à très grand nombre de cycles du fer et de l'acier, PhD dissertation, Université Paris Nanterre, 2013.
[29] Chrysochoos A., Berthel B., Latourte F., Pagano S., Wattrisse B., Weber B., Local energy approach to steel fatigue, Strain. 44 (2008) 327–334. doi:10.1111/j.1475-1305.2007.00381.x.
[30] C. Doudard, C. Sylvain, F. Hild, S. Roux, Identification of heat source fields from infrared thermography: Determination of 'self-heating' in a dual-phase steel by using a dog bone sample, Mechanics of Materials. 42 (2010) 55–62. doi:10.1016/j.mechmat.2009.09.005.
[31] D. Hull, D.J. Bacon, Introduction to Dislocations, Fifth edition, Elsevier, UK, 2011. doi:10.1016/C2009-0-64358-0.
[32] H. Mughrabi, Cyclic slip irreversibilities and the evolution of fatigue damage, Metallurgical and Materials Transactions B. 40 (2009) 431–453. doi:10.1007/s11663-009-9240-4.
[33] Mikell P. Groover, Fundamentals of modern manufacturing; materials, processes, and systems, John Wiley & Sons. Inc, USA, 2007.
[34] B. Luo, M. Li, G. Wang, F. Tan, J. Zhao, C. Sun, Strain rate and hydrostatic pressure effects on strength of iron, Mechanics of Materials. 114 (2017) 142–146. doi:10.1016/j.mechmat.2017.08.001.
[35] W. Bao, X. Ren, Y. Zhang, The characteristics of flow stress and dynamic constitutive model at high strain rates for pure iron, J. Plast. Eng. 5 (2010) 125–129.
[36] Abdel-Salam M. Eleiche, Strain-rate history and temperature effects on the torsional-shear behavior of a mild steel, Experimental Mechanics. 21 (1981) 285–294. doi:https://doi.org/10.1007/BF02325768.
[37] Bao W., Experimental research on the dynamic constitutive relation of pure iron at elevated temperatures and high strain rates, Journal of Mechanical Engineering. 46 (2010) 74. doi:10.3901/JME.2010.04.074.
[38] J.D. Campbell, W.G. Ferguson, The temperature and strain-rate dependence of the shear strength of mild steel, The Philosophical Magazine: A Journal of Theoretical Experimental and Applied Physics. 21 (1970) 63–82. doi:10.1080/14786437008238397.
[39] Z. Huang, Endommagement des aciers au C-Mn en fatigue oligocyclique et gigacyclique. PhD dissertation. Université Paris Nanterre. (2010).

[40] D. Wagner, N. Roubier, C. Prioul, Measurement of sensitivity to dynamic strain aging in C–Mn steels by internal friction experiments., Materials Science and Technology. 22 (2006) 301–307. doi:10.1179/174328406X86155.
[41] Z. Huang, D. Wagner, C. Bathias, Effect of carburizing treatment on the “fish eye” crack growth for a low alloyed chromium steel in Very High Cycle Fatigue, Materials Science and Engineering: A. 559 (2013) 790–797. doi: 10.1016/j.msea.2012.09.025.
[42] H. Mughrabi, K. Herz, X. Stark, Cyclic deformation and fatigue behaviour of α-iron mono- and polycrystals, Int J Fract. 17 (1981) 193–220. doi:10.1007/BF00053520.
[43] A. Chrysochoos, O. Maisonneuve, G. Martin, H. Caumon, J.. Chezeaux, Plastic and dissipated work and stored energy, Nuclear Engineering and Design. 114 (1989) 323–333. doi:10.1016/0029-5493(89)90110-6.
[44] D. Rittel, L.H. Zhang, S. Osovski, The dependence of the Taylor–Quinney coefficient on the dynamic loading mode, Journal of the Mechanics and Physics of Solids. 107 (2017) 96–114. doi:10.1016/j.jmps.2017.06.016.
[45] P. Knysh, Y.P. Korkolis, Determination of the fraction of plastic work converted into heat in metals, Mechanics of Materials. 86 (2015) 71–80. doi:10.1016/j.mechmat.2015.03.006.
[46] F.H. Norton, The creep of steel at high temperatures, McGraw-Hill Book Company, New York, 1929.